Mechanics of Materials 175 (2022) 104482

Contents lists available at ScienceDirect

Mechanics of Materials

journal homepage: www.elsevier.com/locate/mechmat

Editor Invited Article

Instability-induced patterns and their post-buckling development in soft particulate composites

Dean Chen [a], Nitesh Arora [a], Yuhai Xiang [a], Jian Li [b,c], Viacheslav Slesarenko [d], Stephan Rudykh [a,e,*]

[a] Department of Mechanical Engineering, University of Wisconsin–Madison, WI, 53706, United States
[b] Joint International Research Laboratory of Key Technology for Rail Traffic Safety, Central South University, Changsha, 410075, China
[c] Department of Civil and Environmental Engineering, Massachusetts Institute of Technology, Cambridge, MA, 02139, United States
[d] Cluster of Excellence LivMatS @ FIT – Freiburg Center for Interactive Materials and Bioinspired Technologies, University of Freiburg, Georges-Köhler-Allee 105, D-79110, Freiburg, Germany
[e] School of Mathematical and Statistical Sciences, University of Galway, University Road, Galway, Ireland

A B S T R A C T

In this paper, we investigated elastic instabilities in soft particulate composites under finite strains. Through our numerical analysis, we find distinct instability modes developing in the composites upon the critical deformation level. In particular, fully predetermined by its initial geometry, the microstructures transform into (i) strictly doubled periodicity, (ii) seemingly non-periodic state, or (iii) longwave pattern. The latter may give rise to highly ordered domain formations. We analyze the various mechanisms leading to the development of the different instability modes and specifically focus on the seemingly non-periodic one. We illustrate the distinct features of their corresponding eigenmodes obtained from the Bloch-Floquet analysis. We further employ the quasi-convexification analysis and examine the energy landscapes of the soft composites developing the different instability modes. Finally, we examine the development of the predicted instability modes in the post-buckling regime. We find that, depending on the characteristic critical wavenumber, the post-buckling patterns can significantly diverge from those predicted by the Bloch-Floquet analysis. In the post-buckling regime, the instabilities may develop into various scenarios: from a combination of different repeating inclusion sets to disordered, seemingly chaotic patterns.

1. Introduction

Soft composites can experience elastic instabilities leading to their microstructure transformations. Recently, the phenomenon has been employed for designing materials with tunable and switchable properties; examples include tunable bandgap materials (Li et al., 2019c; Rudykh and Boyce, 2014; Shan et al., 2014; Wang et al., 2014; Gao et al., 2019), metamaterials exhibiting negative group velocity states (Slesarenko et al., 2018; Arora et al. (2022)), and negative Poisson's ratio or auxetic materials (Bertoldi et al., 2008; Mullin et al., 2007; Li et al., 2018b; Li et al., 2019b; Li et al., 2019c; Li and Rudykh, 2019b).

To predict the onset of instabilities, the framework of the linearized small motions superimposed on finitely deformed solids is frequently used (Ogden, 1997). The onset of macroscopic or longwave instabilities can be identified with the help of the loss of ellipticity analysis (see, for example, Merodio and Ogden, 2002, 2003, 2005; El Hamdaoui et al., 2018; Melnikov et al., 2021). For composite materials, the analysis requires the determination of the effective tensor of elastic moduli, which can be computed via numerical (Bruno et al., 2010; Greco and Luciano, 2011; Greco et al., 2021) or analytical homogenization schemes (Rudykh and Debotton, 2012). Alternatively, phenomenological models can be used directly to compute the tensor of elastic moduli and provide the deformation limits for material stability (Merodio and Ogden, 2002; Merodio and Pence, 2001).

However, the so-called microscopic instabilities developing at finite wavelengths can occur earlier than the longwave one (Geymonat et al., 1993). To predict the onset of microscopic instability and identify the critical deformation level and wavelength, the Bloch-Floquet analysis superimposed on the finitely deformed state is typically used (Bertoldi et al., 2008; Slesarenko and Rudykh, 2017). We note the equivalence of the longwave limit in the Bloch-Floquet analysis and the loss of ellipticity condition (Geymonat et al., 1993).

Rudykh and Debotton (2012) utilized micromechanics-based homogenization to predict the macroscopic instability in transversely isotropic (TI) fiber composites (FCs). Li et al. (2013) experimentally observed the microscopic and macroscopic instability phenomena of multi-layered composites under plane strain conditions via 3D-printed layered materials. Galich et al. (2018) studied the influence of the

* Corresponding author. Department of Mechanical Engineering, University of Wisconsin–Madison, WI 53706, United States.
E-mail address: rudykh@wisc.edu (S. Rudykh).

https://doi.org/10.1016/j.mechmat.2022.104482
Received 14 August 2022; Accepted 24 September 2022
Available online 12 October 2022
0167-6636/© 2022 Elsevier Ltd. All rights reserved.

periodic fiber distribution on instabilities and shear wave propagation in 3D fiber composites. Arora et al. (2019) examined the influence of the inhomogeneous interphases in 3D-printed soft laminates on their stability. Li et al. (2018a) experimentally investigated the elastic instabilities in 3D-printed fiber composites and observed the transition from small wavelength wavy patterns to the long-wave mode. Li et al. (2019c) analyzed the elastic instability in compressible laminate, reporting the stabilization effect of the phase compressibility. Slesarenko and Rudykh (2016) utilized the visco-hyperelastic behavior of the phase materials in soft composites (Xiang et al., 2020a, 2020b) to achieve the tunability of the wavy patterns via variable strain rates. Constraining the equivalent 3D FC into the in-plane setting, the stability of the 2D system of fiber cross-section has been examined (see, for example, the numerical study Triantafyllidis et al. (2006), and references therein) numerically predicting microscopic or macroscopic instabilities in the particulate composite with circular inclusions (distributed periodically in square and diagonal unit cells) under combined in-plane loadings and for various volume fractions; Michel et al. (2010) reexamined the problem and added a comparison of the macroscopic stability of the composite with a random distribution of particles (including circular and elliptical ones) under similar combined in-plane loadings.

As we shall show, in the particulate composite systems, the important instability characteristics are significantly influenced by the periodicity parameters of the inclusion distributions, affecting both the critical strain and wavelength. Furthermore, the instability modes experience significant alterations in the *post-buckling* regime.

Recently, Li et al. (2019a) reported the experimental observations of the formation of wavy chain patterns in soft particulate composites; moreover, the pattern formation can be controlled by a magnetic field (Goshkoderia et al., 2020a). Motivated by the experimental observations, in this study, we numerically examined the instability-induced patterns in soft particulate composites via (i) *Bloch-Floquet*, (ii) *quasi-convexification*, and (iii) direct *post-buckling* analyses. First, we start by examining the influence of the instability characteristics such as critical strain and wavenumber on the initial geometrical parameters of the periodic microstructure. We numerically realize that the influence could be the manifestation of two different buckling behaviors in the soft particulate systems. We then further focused on the phenomenon of microstructure transformation from its initial geometry into the corresponding instability modes, where we found the typical buckling patterns with (i) the longwave periodicity, (ii) strictly doubled periodicity, and (iii) seemingly non-periodic state. We also analyzed the so-called energy landscapes of the finitely deformed particulate composite, illustrating the microstructure transformation from the view of their energy responses. Finally, we also examined the development of the predicted instability modes in the *post-buckling* regime. In particular, we examine the transition instability modes predicted by the Bloch-Floquet analysis. We shall show that, depending on the characteristic critical wavenumber, the post-buckling instability pattern can significantly differ from those predicted by the Bloch-Floquet analysis.

2. Theoretical background

Consider a continuum body with each point identified with its position vector $\boldsymbol{X}$ in the undeformed configuration and $\boldsymbol{x}$ in the deformed configuration. The corresponding mapping function is $\boldsymbol{x} = \boldsymbol{\chi}(\boldsymbol{X}, t)$. The deformation gradient $\boldsymbol{F}$ is defined as $\boldsymbol{F} = \partial \boldsymbol{x}/\partial \boldsymbol{X}$, and its determinant is $J = det\, \boldsymbol{F} > 0$. For a hyperelastic material, the constitutive behavior is defined by elastic strain energy density function, so that the first Piola-Kirchhoff stress tensor is

$$\boldsymbol{P} = \frac{\partial W(\boldsymbol{F})}{\partial \boldsymbol{F}}. \tag{1}$$

For an incompressible material, $J = 1$, Eq. (1) modifies as

$$\boldsymbol{P} = \frac{\partial W(\boldsymbol{F})}{\partial \boldsymbol{F}} - p\boldsymbol{F}^{-T}, \tag{2}$$

where p is an unknown Lagrange multiplier. Consider quasi-static deformation in the absence of body forces. The corresponding equilibrium equation in the undeformed configuration reads

$$Div\, \boldsymbol{P} = \boldsymbol{0}. \tag{3}$$

To analyze the material stability, we consider incremental deformations superimposed on a finitely deformed state. The corresponding linearized constitutive law is

$$\dot{\boldsymbol{P}} = \mathbb{A} : \dot{\boldsymbol{F}}, \tag{4}$$

where $\dot{\boldsymbol{F}}$ is an incremental change in the deformation gradient, defined as $\dot{\boldsymbol{F}} = Grad\, \boldsymbol{u}$, and $\boldsymbol{u}$ is the incremental displacement. $\dot{\boldsymbol{P}}$ is the corresponding change in the first Piola-Kirchhoff stress tensor, and $\mathbb{A}$ is the tensor of elastic moduli, defined as

$$\mathbb{A} = \frac{\partial^2 W}{\partial \boldsymbol{F} \partial \boldsymbol{F}}. \tag{5}$$

Under the assumption that $\mathbb{A}_{i\alpha j\beta}$ is independent of $\boldsymbol{X}$, the incremental equilibrium equation can be written as

$$\mathbb{A}_{i\alpha j\beta} \frac{\partial^2 u_j}{\partial X_\alpha \partial X_\beta} = 0. \tag{6}$$

For incompressible materials, Eq. (6) modifies to

$$\mathbb{A}_{i\alpha j\beta} \frac{\partial^2 u_j}{\partial X_\alpha \partial X_\beta} + \frac{\partial \dot{p}}{\partial X_i} = 0, \tag{7}$$

where $\dot{p}$ is a variation in p.

The incompressibility condition implies

$$\nabla \cdot \boldsymbol{u} = 0. \tag{8}$$

By application of the chain rule, the incremental equilibrium Eq. (7) can be written in the current configuration as

$$\mathbb{A}^0_{ipjq} \frac{\partial^2 u_j}{\partial x_p \partial x_q} + \frac{\partial \dot{p}}{\partial x_i} = 0, \tag{9}$$

where

$$\mathbb{A}^0_{ipjq} = J^{-1} F_{p\alpha} F_{q\beta} \mathbb{A}_{i\alpha j\beta}. \tag{10}$$

We seek a solution for Eq. (9) in the form

$$\boldsymbol{u} = \widehat{\boldsymbol{m}} e^{ik\boldsymbol{x}\cdot\widehat{\boldsymbol{n}}}, \quad \dot{p} = \widehat{p} e^{ik\boldsymbol{x}\cdot\widehat{\boldsymbol{n}}}, \tag{11}$$

where k is a wavenumber, $\widehat{\boldsymbol{m}}$ and $\widehat{\boldsymbol{n}}$ are unit vectors.

The incompressibility condition Eq. (8) leads to the requirement

$$\widehat{\boldsymbol{m}} \cdot \widehat{\boldsymbol{n}} = 0. \tag{12}$$

Substitution of Eq. (11) into Eq. (9) yields

$$\boldsymbol{Q}\widehat{\boldsymbol{m}} + i\widehat{p}\widehat{\boldsymbol{n}} = \boldsymbol{0}, \tag{13}$$

where $\boldsymbol{Q}$ is the acoustic tensor with the components defined as

$$Q_{ij} = \mathbb{A}^0_{ipjq} \widehat{n}_p \widehat{n}_q. \tag{14}$$

The associated strong ellipticity condition implies

$$Q_{ij} \widehat{m}_i \widehat{m}_j \equiv \mathbb{A}^0_{ipjq} \widehat{n}_p \widehat{n}_q \widehat{m}_i \widehat{m}_j > 0. \tag{15}$$

Thus, the loss of stability is associated with the condition $Q_{ij}\widehat{m}_i\widehat{m}_j = 0$. In the context of the heterogeneous composites, the loss of ellipticity analysis requires the determination of the effective tensor of elastic moduli, and, thus, identifies the onset of longwave or macroscopic

instabilities. To predict the instabilities developing at the length scales comparable with the composite microstructures, the Bloch-Floquet analysis of small amplitude deformations (superimposed on finite deformation) can be employed. While analytical solutions can be derived for some hyperelastic composites – such as periodic laminates – typically, the analysis is performed numerically with the help of the Finite Element (FE) method (Bertoldi et al., 2008).

3. Bloch–Floquet microscopic instability analysis

3.1. Numerical implementation of the Bloch-Floquet microscopic instability analysis

Consider a composite with the 2D rectangular primitive unit cell as shown in Fig. 1. The rectangular unit cell is enclosed by four boundaries (*AB*, *CD*, *AC*, *BD*), defined by nodes *A*, *B*, *C*, *D*. The width and length of the primitive unit cell are denoted by a and b, respectively. The geometry can be parameterized through periodicity aspect ratio $\eta = a/b$ and inclusion spacing ratio $\xi = d/b$, where d is the diameter of the inclusion. The numerical analysis has been implemented in the finite element code in COMSOL 5.4a, as follows.

First, the in-plane unidirectional compression is applied by imposing the periodic boundary conditions on boundary pairs *AB* and *CD* as

$$\boldsymbol{u}_{AB} - \boldsymbol{u}_{CD} = (\overline{\boldsymbol{F}} - \boldsymbol{I})\left(\boldsymbol{X}|_{AB} - \boldsymbol{X}|_{CD}\right) = \overline{\boldsymbol{H}}\left(\boldsymbol{X}|_{AB} - \boldsymbol{X}|_{CD}\right), \tag{16}$$

where $\boldsymbol{u}_{AB}$ and $\boldsymbol{u}_{CD}$ represents the displacement of an arbitrary pair of source and destination points periodically located on boundary pair *AB* and *CD*, respectively; $\overline{\boldsymbol{F}}$ denotes the average deformation gradient, and $\overline{\boldsymbol{H}} = \overline{\boldsymbol{F}} - \boldsymbol{I}$ denotes the average displacement gradient. Thus, the applied uniaxial compression loading is defined as

$$\overline{\boldsymbol{H}} = H_{11}\boldsymbol{e}_1 \otimes \boldsymbol{e}_1 + (\lambda - 1)\boldsymbol{e}_2 \otimes \boldsymbol{e}_2, \tag{17}$$

where the loading level is prescribed via the average compressive strain $\varepsilon = 1 - \lambda$. Note that H_{11} is not prescribed and is determined by the traction-free boundary condition $P_{11} = 0$.

Second, we employ the Bloch–Floquet analysis superimposed on the deformed state(Bertoldi et al., 2008). The Floquet periodic conditions relate the incremental displacement fields $\boldsymbol{u}$ via

$$\boldsymbol{u}(\boldsymbol{X} + \boldsymbol{R}) = \boldsymbol{u}(\boldsymbol{X})e^{i\boldsymbol{K}\cdot\boldsymbol{R}}, \tag{18}$$

where $\boldsymbol{K} = K_1\boldsymbol{e}_1 + K_2\boldsymbol{e}_2$ is the Bloch wave vector, and $\boldsymbol{R} = R_1 a\boldsymbol{e}_1 + R_2 b\boldsymbol{e}_2$ is a vector that denotes the initial periodicity of the composite with arbitrary integers R_1, R_2. In FEA, the Bloch–Floquet analysis is performed by solving the eigenvalue problem with Floquet boundary conditions imposed on the boundary pairs of the primitive unit cell read as $\boldsymbol{u}_{AB} = \boldsymbol{u}_{CD}e^{-i\boldsymbol{K}\cdot(\boldsymbol{R}_{AB}-\boldsymbol{R}_{CD})}$ and $\boldsymbol{u}_{BD} = \boldsymbol{u}_{AC}e^{-i\boldsymbol{K}\cdot(\boldsymbol{R}_{BD}-\boldsymbol{R}_{AC})}$. Here, the normalized components of the wavenumber are $k_1 = K_1 a/2\pi$ and $k_2 = K_2 b/2\pi$ in the undeformed configuration. Through the numerical analysis, we determine the lowest critical loading level (critical strain ε^{cr}) for which a zero eigenvalue occurs at the corresponding critical wavenumber k^{cr} (k_1^{cr} or k_2^{cr}). We refer to the cases with $k^{cr} \to 0$ as the longwave or macroscopic instability, and microscopic instabilities otherwise. We note that – throughout our calculations – the instabilities are found to develop only in the direction of compression (direction of $\boldsymbol{e}_2$) for all considered cases. Therefore, we report the corresponding critical wavenumber as $k^{cr} = k_2^{cr}$.

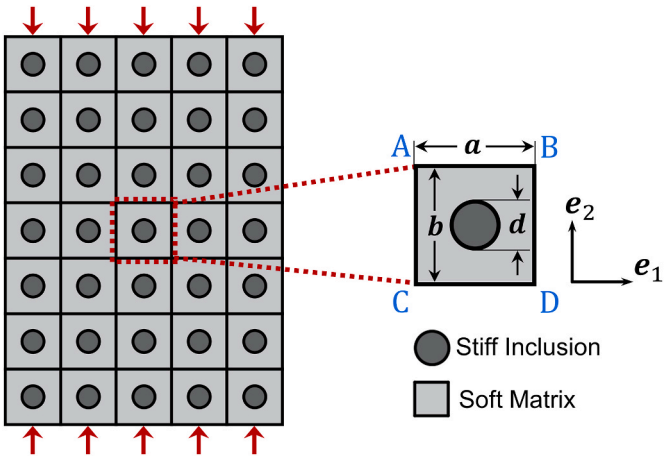


Fig. 1. Schematic composite microstructure with stiff circular inclusions periodically distributed in soft matrices.

The behavior of the stiff inclusion and soft matrix materials is described by the nearly incompressible neo-Hookean strain energy density function, namely

$$\mathrm{W}^{(\mathrm{r})} = \frac{\mu^{(\mathrm{r})}}{2}(\bar{I}_1 - 3) + \frac{\kappa^{(\mathrm{r})}}{2}(J-1)^2, \tag{19}$$

where $\mu^{(\mathrm{r})}$ is the initial shear modulus, $\kappa^{(\mathrm{r})}$ is the bulk modulus, and $I_1 = \mathrm{tr}\boldsymbol{C}$ is the first invariant of the right Cauchy-Green tensor $\boldsymbol{C} = \boldsymbol{F}^{\mathrm{T}}\boldsymbol{F}$. The superscript (r) indicates the properties of different material phases; for example, (r) = (m) denotes the stiff inclusion phases, and (r) = (i) denotes the soft matrix phases. We introduce the ratio $\Lambda = \kappa^{(\mathrm{r})}/\mu^{(\mathrm{r})}$ representing the material compressibility, and assign a high ratio, $\Lambda = 10^3$, to maintain a nearly incompressible behavior of the material. We select the inclusion-to-matrix ratio of shear moduli $\mu^{(\mathrm{i})}/\mu^{(\mathrm{m})} = 10^3$. Therefore, stiff inclusions almost do not deform, and the deformation is mostly accommodated by the soft matrix.

3.2. Dependence of critical strains on geometric parameters

We start by examining the influence of the instability characteristics such as critical strain and wavenumber on the initial geometrical parameters of the periodic microstructure. Fig. 2 shows the dependence of the critical strain on the periodicity aspect ratio η for various fixed values of the inclusion spacing ratios ξ from 0.1 to 0.9. Note that, the admissible geometries are restricted by $d < b$ and $d < a$, thus, limited the parameter space as $\eta > \xi$. Here and thereafter, the dotted and continuous curves correspond to longwave (or macroscopic) and microscopic instabilities, respectively.

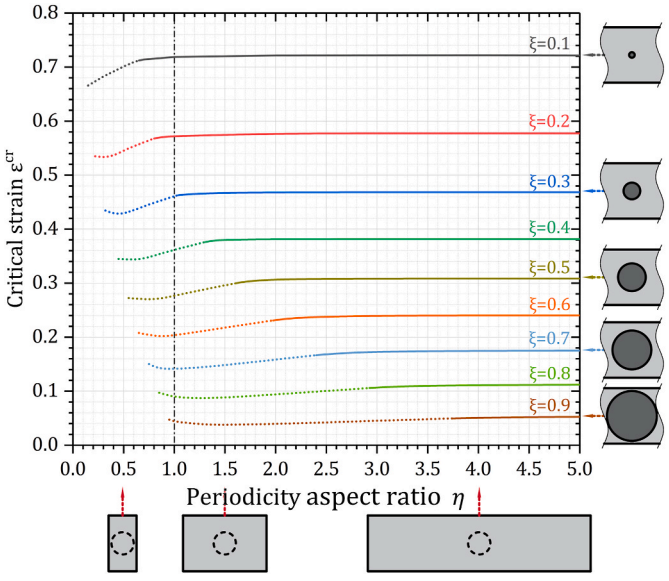


Fig. 2. The dependence of critical strain on periodicity aspect ratio with various spacing ratios. Dotted and continuous curves correspond to macroscopic and microscopic instabilities, respectively.

We observe that the composites with higher spacing ratios experience instabilities at lower compressive strains. In these composites, the inclusions are placed more closely in the compressive direction. Thus, the stiff inclusions are brought into their strong interactions at lower strain levels leading to earlier instability development. Interestingly, the dependence of the critical strain on the spacing periodicity ratio alters with a change in the inclusion spacing ratio. For composites with small spacing ratios, the critical strain ε^{cr} increases monotonically with an increase in η (see, for example, the black curve corresponding to $\xi = 0.1$ in Fig. 2). This behavior, however, changes to a non-monotonic one in the composite with low-to-moderate spacing ratios. Their curves decrease initially; however, after reaching their local minima, the critical strain increases with a further increase in the periodicity aspect ratio and finally converges to a plateau. For example, for the composite with $\xi = 0.3$ (the blue curve in Fig. 2), ε^{cr} decrease initially, after reaching its local minimum $\varepsilon^{cr} = 0.426$ at $\eta = 0.45$, the curve starts to increase and eventually converges to a plateau after $\eta > 1.035$. The asymptotic values of the plateaus correspond to those initial configurations with an isolated or single column of inclusions embedded in the soft matrix.

This non-monotonic dependence is the manifestation of two different dominating buckling behaviors in the soft particulate systems. In particular, the composites with high periodicity aspect ratios exhibit the laminate-like behavior (with the stiffer layers reinforced by the stiff inclusions); in these composites, the critical strain decreases as the periodicity aspect ratio decreases (corresponding to an increase in the effective volume fraction of the analogous reinforced layer). However, as the periodicity aspect ratio is decreased further, the buckling behavior changes as the inclusions are introduced into additional horizontal interactions. The introduced horizontal frustration forces the soft particulate system to seek a different buckling mechanism requiring higher strain levels. The transition in the buckling behavior can be illustrated by considering the soft composites with $\xi = 0.6$ (see the orange curve in Fig. 2). For the configurations with higher periodicity aspect ratios ($\eta \gtrsim 0.85$), the composites exhibit the laminate-like buckling behavior, and the critical strain decreases with a decrease in the inclusions spacing ratio. The behavior starts changing in the configurations with $\eta \approx 0.85$, and the critical strain increases with a decrease in η. For the composites with $\xi = 0.6$, the transition point corresponding to the local minimum of the curve is $\eta \approx 0.85$. The composites with large inclusion spacing ratios (larger inclusions) are characterized by a more narrow range of the periodicity aspect ratios, where they exhibit the laminate-like buckling behavior (accompanied by a decrease in the critical strain with a decrease in the periodicity aspect ratio). This is due to the fact that the additional horizontal particle interactions are more likely to be introduced in the composites with larger stiff inclusions. Correspondingly, the transition point shifts towards the large periodicity aspect ratio values with an increase in ξ. For example, the composites with $\xi = 0.3$ and 0.9 have their transition points at $\eta \approx 0.45$ and $\eta \approx 1.5$, respectively.

We further illustrate the transition between these two different system behaviors in Fig. 3 for the soft composites with $\xi = 0.6$ and $\eta = 0.62$, 0.85, 1.5, and 2. Fig. 3 shows the deformation field distribution with the vertical strain component ε_{22}. When the compressive deformation is high enough, the inclusions are pushed close to each other in the compressive direction. The composite with higher periodicity aspect ratios (for example, the composite with $\eta = 2$ in Fig. 3) forms the columns of compactly lined up inclusions in the deformed configuration. The deformed system creates the analogous "effective stiffer layers" and "softer matrix layers" (see the deformed composite with $\eta = 2$ in Fig. 3). The particulate composite is observed to exhibit laminate-like buckling behavior. When the periodicity aspect ratio is decreased (compare the composite cells with $\eta = 2$ and 1.5 in Fig. 3), the effective stiffer layers are placed closer to each other, resulting in an increase in the analogous volume fraction of the effective stiffer phase. Similar to the laminate buckling behavior (Li, Slesarenko, et al., 2019c; Li et al., 2013), the composites are characterized by a decrease in the critical strain as the periodicity ratio is decreased. In particular, the critical strain decreases from $\varepsilon^{cr} = 0.231$ to $\varepsilon^{cr} = 0.217$ in the composites with η decreased from 2 to 1.5.

As the periodicity aspect ratio further decreases, the composite configurations enter into the transition buckling behavior. Such configuration is illustrated in Fig. 3 for the composite with the periodicity aspect ratio $\eta = 0.85$. The columns of stiff inclusions are placed close to each other so that the inclusions are introduced into additional horizontal interactions. This is illustrated by the deformation distribution field showing the strong interaction of the stiff inclusions in both vertical and horizontal directions. The proximity of the stiff inclusions columns hinders the buckling development and makes the structure more stable. This mechanism manifests in the increase of the critical strain when the periodicity aspect ratio is decreased further (beyond the transition minimum point). Thus, for example, the critical strain increases from 0.201 to 0.211 in the soft composites with $\eta = 0.85$ and $\eta = 0.62$ (shown in Fig. 2).

3.3. Dependence of critical wavenumber on initial microstructure geometric parameters

Finally, we recall the essential feature of the failure curves, namely, the existence of a transition from macroscopic (or longwave) to microscopic instability mode occurring at a critical threshold value η^{th}. For example, the composite with $\xi = 0.6$ transits from macroscopic to microscopic instability at the threshold value is $\eta^{th} \approx 1.975$, and the threshold values gradually increase with an increase in the spacing ratio. This transition of instability modes is characterized by the corresponding change in the critical wavenumber.

Fig. 4 shows the dependence of the critical wavenumber k^{cr} on the periodicity aspect ratio η, for various fixed values of the inclusion spacing ratios ξ from 0.1 to 0.9. We observe in Fig. 4 that the curves are characterized by the existence of macroscopic or longwave instability ($k^{cr} \to 0$) in the initial ranges of their periodicity aspect ratio lower than their threshold values η^{th}. The threshold value – after which a switch

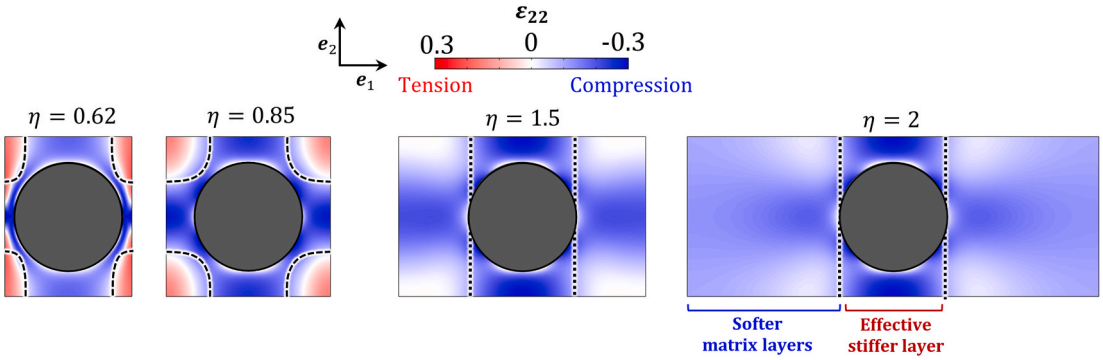


Fig. 3. Distribution of strain field, ε_{22}, in the composite with $\xi = 0.6$ under the applied average compressive strain $\varepsilon = 0.24$ with various periodicity aspect ratios.

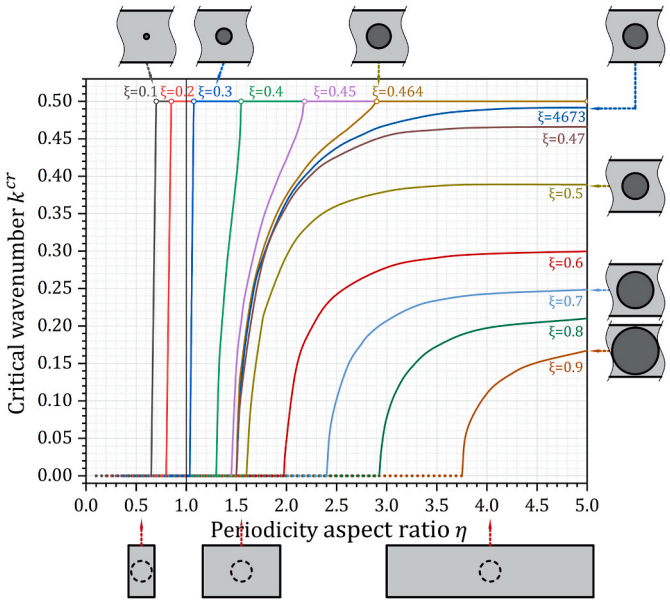


Fig. 4. The dependence of critical wavenumber on the periodicity aspect ratio with various spacing ratios. Dotted and continuous curves correspond to macroscopic and microscopic instabilities, respectively.

from macroscopic to microscopic buckling mode happens – is dictated by the initial spacing ratio value ξ. This transition from macro- to micro-instability modes happens rather rapidly in the composites with small initial spacing ratios. For example, in the composite with $\xi = 0.2$ (see the red curve in Fig. 4), the wavenumber suddenly switches from $k^{cr} = 0$ to 0.5 at the threshold value $\eta^{th} \approx 0.8$. In the composites with higher periodicity aspect ratios, however, gradual transitions are observed; the corresponding critical wavenumbers continuously increase from zero until reaching the plateau value at the corresponding threshold value. For instance, in the composites with $\xi = 0.45$ (see the violet curve in Fig. 4), the wave number k^{cr} increases after the threshold value $\eta^{th} = 1.45$, and it reaches the maximum bound level of 0.5 at $\eta = 2.18$. After reaching the threshold value, the critical wavenumber does not change with a further increase in the periodicity aspect ratio η. For the composites with even higher spacing ratios, the critical wavenumber k^{cr} does not reach the upper bound value of 0.5; instead, the wavenumber approaches a lower-level plateau for a high enough η. For example, in the composites with $\xi = 0.6$, the critical wavenumber increases after the threshold value $\eta^{th} = 1.975$, followed by the curve flattening and asymptotically reaching the plateau value with $k^{cr} \to 0.31$.

We schematically illustrate the corresponding instability patterns in Fig. 5. Prior to the onset of instabilities, the composite's periodicity is defined by the *initial* primitive cell (shown in the left part in Fig. 5) with the initial periodicity $l_1^0 = a$ and $l_2^0 = b$. Once the bifurcation occurs, the initial periodicity may break, and the composite attains a new periodicity with an *enlarged* primitive cell characterized by critical wavelength l_1^{cr} and l_2^{cr} (defined in the undeformed configuration). Recall that our calculations indicate that the onset of instabilities develops along the compressive direction, and the horizontal periodicity does not change upon buckling, namely, $l_1^{cr} \equiv l_1^0$; the vertical periodicity, however, does change with the onset of instability; therefore, here and thereafter, we only consider l_2^{cr} component of the critical wavelength and report l_2^{cr} as l^{cr} and l_2^0 as l^0 for simplification. For instability patterns, the following cases can occur. First, the enlarged primitive cell consists of an *integer* number of initial primitive cells. In this case, the critical wavelength is $l^{cr} = pl^0$ where p is an integer defining the number of initial primitive cells included in the enlarged primitive cell; the unit cell number can be obtained as $p = 1/k^{cr}$. For example, for the composite with $\xi = 0.45$ and $\eta = 1.6$, $k^{cr} = 0.25$, so that the enlarged primitive cell consists of $p = 4$ with an expected wavy pattern, including four inclusions in the period (see the right part in Fig. 5). A similar case with $k^{cr} = 0.5$ (for example, the cases with $\xi = 0.45$ and $\eta > 2.18$) is also illustrated in Fig. 5. In this case, a wavy pattern with two inclusions in the period is expected to develop upon the onset of instability. Similar to the above examples, the composites with their critical wavenumbers corresponding to $p = N($ where $N = 1, 2, 3 \ldots)$ may develop a wavy pattern with critical wavelength $l^{cr} = pl^0$, including N incisions in its period. We note, however, that the critical wavenumbers can be continuous functions of η (see, for example, the curves for the composites with $\xi = 0.45$ in Fig. 4). Therefore, an infinite number of instability configurations with *non-integer* values of $1/k^{cr}$ are admissible through tuning the initial periodicity parameters. Fig. 5 schematically illustrates such a case of the composite with $\xi = 0.4$, $\eta = 1.546$, the corresponding critical wavenumber is $k^{cr} \approx 0.49$. However, $1/k^{cr} \approx 2.04$ is indeed not an integer number, which we denote as $p' = 1/k^{cr}$ (to distinguish it from the cases with an integer number of unit cells). The corresponding enlarged primitive cell (consisting of an integer number of initial primitive cells) may be constructed, if there exist a large enough integer number n such that $p = np'$ is an integer. We note, however, that consideration may be sensitive to the accuracy of the results of the Bloch-Floquet analysis, namely, the accuracy of the critical wavenumber k^{cr} (and, hence, of p'). Thus, the composites (that are characterized by their critical wavenumber in the range $0 < k^{cr} < 0.5$) exhibit seemingly non-periodic instability patterns.

Next, we examine the seemingly non-periodic instability patterns via corresponding eigenmodes of the composites at the critical strains. Fig. 6 shows the eigenmodes of the composites at the critical strains with fixed spacing ratio $\xi = 0.4$ and various periodicity aspect ratios $\eta = 1.546$, 1.544, 1.54, 1.5, 1.4, and 1.325 corresponding to eigenmodes (1)–(6). For each eigenmode, the colored map shows the relative lateral displacement (u_1) distribution. Note that, while the numerical analysis is performed on the single unit cell, the eigenmodes are reconstructed via the corresponding Floquet conditions to include a large number of unit cells in each domain (in particular, 50 unit cells are used).

For the composites characterized by smaller critical wavenumbers (see, for example, case (6) with $k^{cr} \approx 0.134$ corresponding to $p' \approx 7.463$ in Fig. 6), the eigenmodes exhibit wavy shapes with seemingly constant wavelengths. However, the wavelength of the overall wavy mode does not match the periodicity of the inclusion distribution. This mismatch –

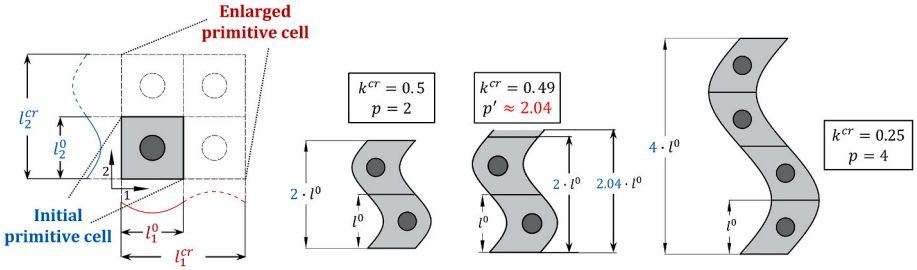


Fig. 5. Schematics of instability patterns based on initial primitive cells and enlarged primitive cells.

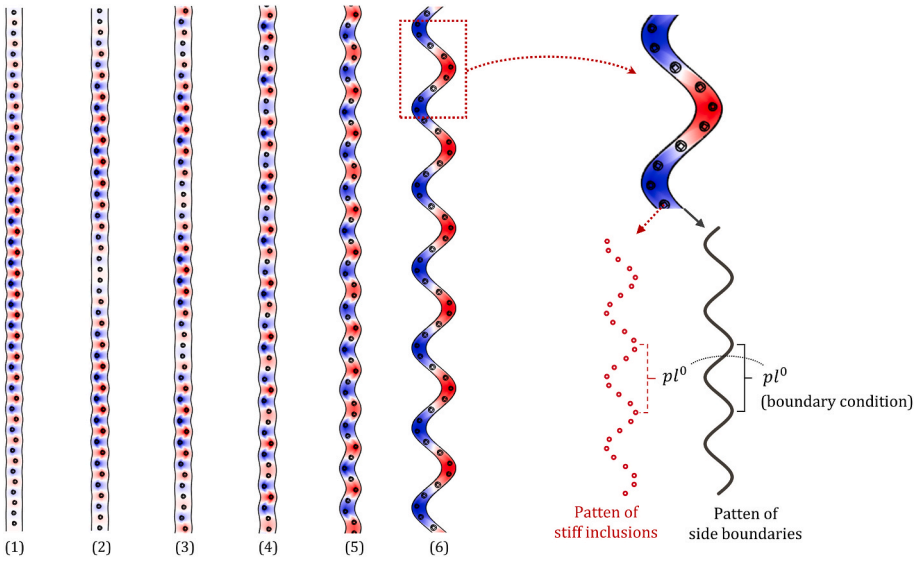


Fig. 6. Eigenmodes of the composites at the critical strains with spacing ratio $\xi = 0.4$ and various periodicity aspect ratios from 1.546 to 1.325.

stemming from the fact that the smallest repeating unit must contain an integer number of inclusions – is illustrated in the schematics for case (6) in the right part of Fig. 6. The wavelength in case (6) is $7.463l^0$; thus, the seemingly full period does not contain an integer number of inclusions; therefore, the actual wavelength may be significantly higher, and its estimate depends on the accuracy of the critical wavenumber determined from the Bloch-Floquet analysis.

Consider the composites developing instabilities with the critical wavenumbers k^{cr} close to 0.5, such as, for example, cases (1)–(3) in Fig. 6. Their eigenmodes exhibit a beat-like phenomenon (Ferrari and Gatti, 1999). For example, case (1), characterized by $k^{cr} \approx 0.491$ ($p \approx 2.04$) in Fig. 6, shows a wave packet with variable magnitudes; the wavelength of the envelope is approximated as $50l^0$. This eigenmode shows the features characterized by a superposition of two wavelets with very close wavelengths: $2.04l^0$ (defined by the critical wavenumber k^{cr}) and $2l^0$ (dictated by the closest integer number of inclusions within the updated primitive cells). This situation is reminiscent of the beat phenomenon with the superposition of two waves with slightly different wavenumbers, resulting in a wavy pattern with variable magnitudes (Ferrari and Gatti, 1999). The envelope of the maxima and minima in the superposed wave can be characterized by the estimated wavenumber $k^{env} \approx 0.5 - k^{cr}$. However, we observe that the composite included in one period of the envelope is still not a smallest repeating unit (see, for example, case (2), characterized by $k^{cr} \approx 0.479$ in Fig. 6, the distribution of the inclusions in one period of envelope curve does not exactly match that in the neighboring periods), and the strict smallest repeating unit should be constructed in a much higher scale.

3.4. Instability mode transitions via initial microstructure geometric parameters

Next, we summarize the results of critical wavenumbers as a surface in the geometrical parameter space of η and ξ in Fig. 7.

In particular, the surface is divided into three sub-domains: (i) the pure red surface on the bottom – labeled as the "longwave" – denotes the geometries for which longwave instabilities develop (with $k^{cr} \to 0$); (ii) the pure blue surface – labeled as the "periodicity doubling" – on the top denotes the microscopic instabilities with constant critical wavenumber $k^{cr} = 0.5$ corresponding to the cases with the initial periodicity being (exactly) doubled upon bifurcation; (iii) the gradient surface – labeled with "transition" – in-between denotes the microscopic instabilities with various k^{cr} from 0 to 0.5, governed by the initial geometric parameters.

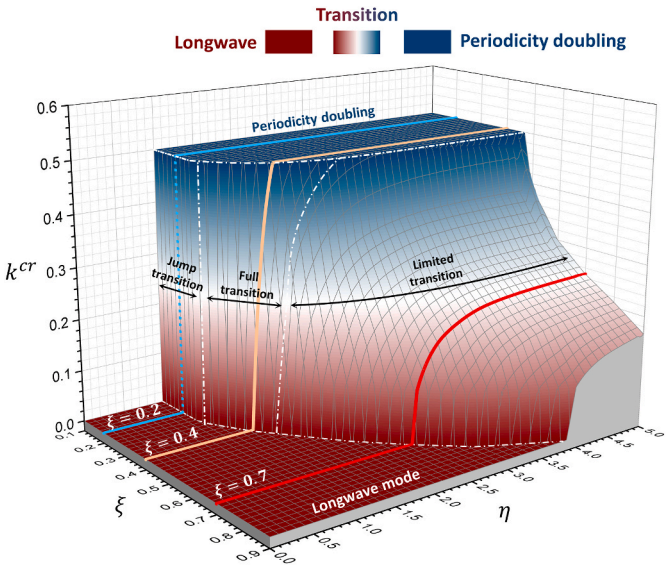


Fig. 7. Surface of critical wavenumber in the space of periodicity aspect and spacing ratio. The red, yellow, and blue curves correspond to the dependence of critical wavenumber on the periodicity aspect ratio with fixed spacing ratios $\xi = 0.7$, $\xi = 0.4$ and $\xi = 0.2$, respectively. (For interpretation of the references to color in this figure legend, the reader is referred to the Web version of this article.)

Moreover, in the transition surface, we can further identify three different transition modes dictated by the initial spacing ratio ξ. First, for the composites with $\xi \lesssim 0.3$, only binary values of the critical wavenumber are possible, namely, either $k^{cr} \to 0$ or $k^{cr} = 0.5$, without any intermediate wavenumber (see, for example, the blue curve corresponding to $\xi = 0.2$ in Fig. 7; the wavenumber jumps from 0 to 0.5 at threshold value $\eta^{th} = 0.85$). Thus, we refer to this transition as the jump-transition mode. Second, for the composites with $0.3 \lesssim \xi \lesssim 0.464$, the transition develops gradually, with the wavenumbers changing from 0 to 0.5. This transition case is illustrated by the yellow curve corresponding to $\xi = 0.4$ in Fig. 7; the critical wavenumber increases continuously after the threshold value $\eta^{th} = 1.325$ and reaches the maximum level of 0.5 at $\eta = 1.548$. We denote this transition as the full-transition mode. Third, in the composites with $0.464 \lesssim \xi \lesssim 1$, the

transition is somewhat similar to the previous case. The important difference, however, is that those composites are limited by their corresponding values of critical wavenumbers and do not attain $k^{cr} = 0.5$. For example, see the red curve corresponding to $\xi = 0.7$ in Fig. 7; here, the curve flattens (after the gradual increase range) and eventually reaches the plateau with $k^{cr} \to 0.248$. We refer to this transition as the limited-transition mode. As discussed above, the beat-like eigenmodes are observed for the composites developing instabilities with k^{cr} close but not equal to 0.5. Since in jump-transition mode we can only find $k^{cr} = 0$ or $k^{cr} = 0.5$, the beat-like eigenmodes are only expected to be found in full-transition and limited-transmission mode, such like $k^{cr} \approx 0.491$ corresponding to $\xi = 0.4$ and $\eta = 1.546$ in the full-transition mode and $k^{cr} \approx 0.454$ corresponding to $\xi = 0.47$ and $\eta = 3$ in the limited-transmission mode.

4. Instability analysis via energy landscapes

Next, we illustrate the so-called energy landscapes of the finitely deformed particulate composite. In the analysis, we calculate the macroscopic response of a single unit cell deformed beyond the possible instability point (similar to the standard post-buckling regime simulations (Li et al., 2019b; Bertoldi et al., 2008)). Then, the quasi-convexification of the calculated elastic strain energy function $W(\boldsymbol{F})$ in the applied deformation gradient $\boldsymbol{F}$ is examined.

A strain energy function $W(\boldsymbol{F})$ is said to be quasi-convex (Morrey, 1952) if

$$W(\boldsymbol{F}) \leq \frac{1}{|D|}\int_{\mathrm{D}} W(\boldsymbol{F} + Grad\ \boldsymbol{u}\ (\boldsymbol{X}))d\boldsymbol{X} \tag{20}$$

for every bounded region D and for every smooth function with compact support $\boldsymbol{u}\ (\boldsymbol{X})$. Note that the quasi-convexification of the energy with the volumetric constraints (such as incompressibility constraint) is rank-one convexification (Conti, 2008). In the following study, we identify the critical conditions for the loss of quasi-convexity or 'relaxation' in the strain energy function.

We consider the composites subjected to simultaneously applied compressive strain and pure shear deformations, the corresponding macroscopic deformation gradient $\overline{\boldsymbol{F}}$ is

$$\overline{\boldsymbol{F}} = H_{11}\boldsymbol{e}_1 \otimes \boldsymbol{e}_1 + \varepsilon \boldsymbol{e}_2 \otimes \boldsymbol{e}_2 \pm \gamma \boldsymbol{e}_1 \otimes \boldsymbol{e}_2 + \boldsymbol{I}, \tag{21}$$

where ε and γ are the compressive strain measure and amount of shear, respectively. Note that H_{11} is determined by the corresponding traction-free boundary condition. The effective (or homogenized) strain energy W stored in the unit cell under prescribed deformations is computed and normalized via

$$\widetilde{W}(\overline{\boldsymbol{F}}) = \frac{1}{\mu^{(m)}}\frac{1}{\Omega_0}\int_{\Omega_0} W(\boldsymbol{X}, \boldsymbol{F})dV_X \tag{22}$$

Next, we compute the energy landscape of the composite cell based on $\widetilde{W}(\varepsilon, \gamma)$ as a function of the compressive strain ε and amount of shear γ. According to the condition of quasi-convexity in Eq. (22), the 'relaxation' or loss of quasi-convexity of the effective energy function is associated with the condition

$$\widetilde{W}(\varepsilon, \gamma) = \widetilde{W}(\varepsilon, \gamma = 0) \tag{23}$$

for any non-zero amount of shear γ. Finally, the lowest compressive strain ε, corresponding to the 'relaxation' of the effective energy function $\widetilde{W}$, is identified as the critical strain level.

Fig. 8 shows an example of the energy landscape in the soft composite with geometrical parameters $\xi = 0.7$ and $\eta = 1$. The effective energy $\widetilde{W}$ is plotted as a surface function of γ and ε in Fig. 8a. Fig. 8b shows the corresponding functions of $\widetilde{W}(\gamma)$ at fixed vales ε (see, for example, the curve corresponding to $\varepsilon = 0.18$ in Fig. 8b and $\widetilde{W}(\varepsilon = 0.18, \gamma)$ in Fig. 8a). We observe that, for curves corresponding to a relatively small strain levels (see, for example, the curve corresponding to $\varepsilon = 0.05$ in Fig. 8b), the effective energy increases with an increase in γ. This indicates that the development of the shearing mode will require additional energy under this level of compression. For curves corresponding to a large enough level of compression (for example, the curve corresponding to $\varepsilon = 0.19$ in Fig. 8b), the energy function decreases with an increase in γ. This indicates that the system can develop the shearing mode without requiring additional energy so that the composite becomes unstable. The onset of instability is identified at the critical strain level ε^{cr}, at which the composite transits from a stable state to an unstable state (see, for example, in Fig. 8b, the critical strain is identified as $\varepsilon^{cr} = 0.141$).

Fig. 9a shows a comparison of the critical strains identified from the energy landscapes (black curves) and that from the Bloch-Floquet analysis (colored curves), where the dependence of the critical strain on the periodicity aspect ratio η is plotted for composites with various fixed values of the spacing ratios $\xi = 0.3$, $\xi = 0.5$ and $\xi = 0.7$. We observe that, the onset of the longwave instability identified by the energy landscape analysis coincides with the one predicted by the Bloch-Floquet analysis (see, for example, the overlapped continuous and

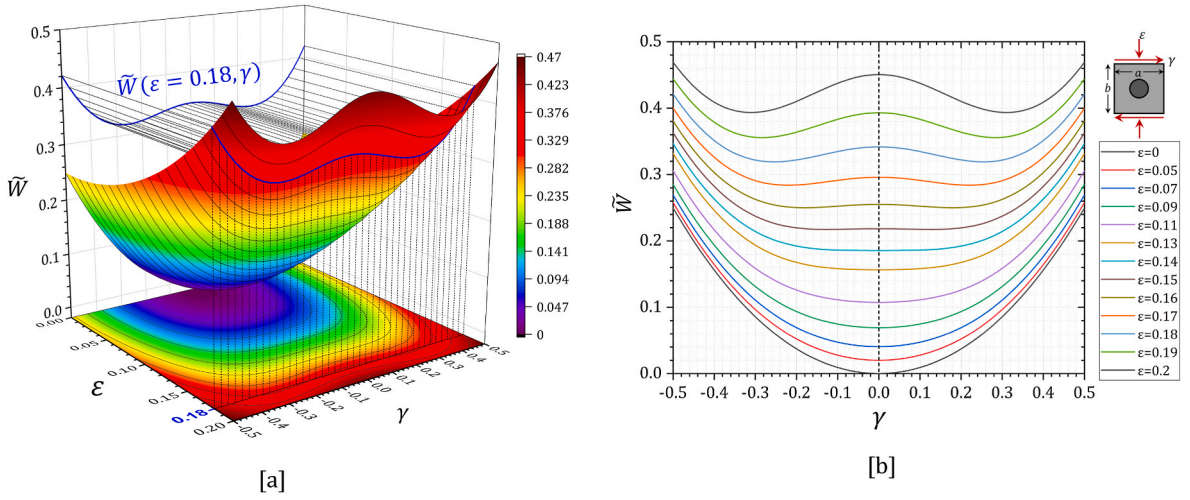


Fig. 8. (a) Landscape of the normalized stored-energy $\widetilde{W}$ as a function of the compressive strain ε and amount of shear γ (corresponding to $\xi = 0.7$ and $\eta = 1$). (b) The curves of normalized stored energy with various γ and fixed ε.

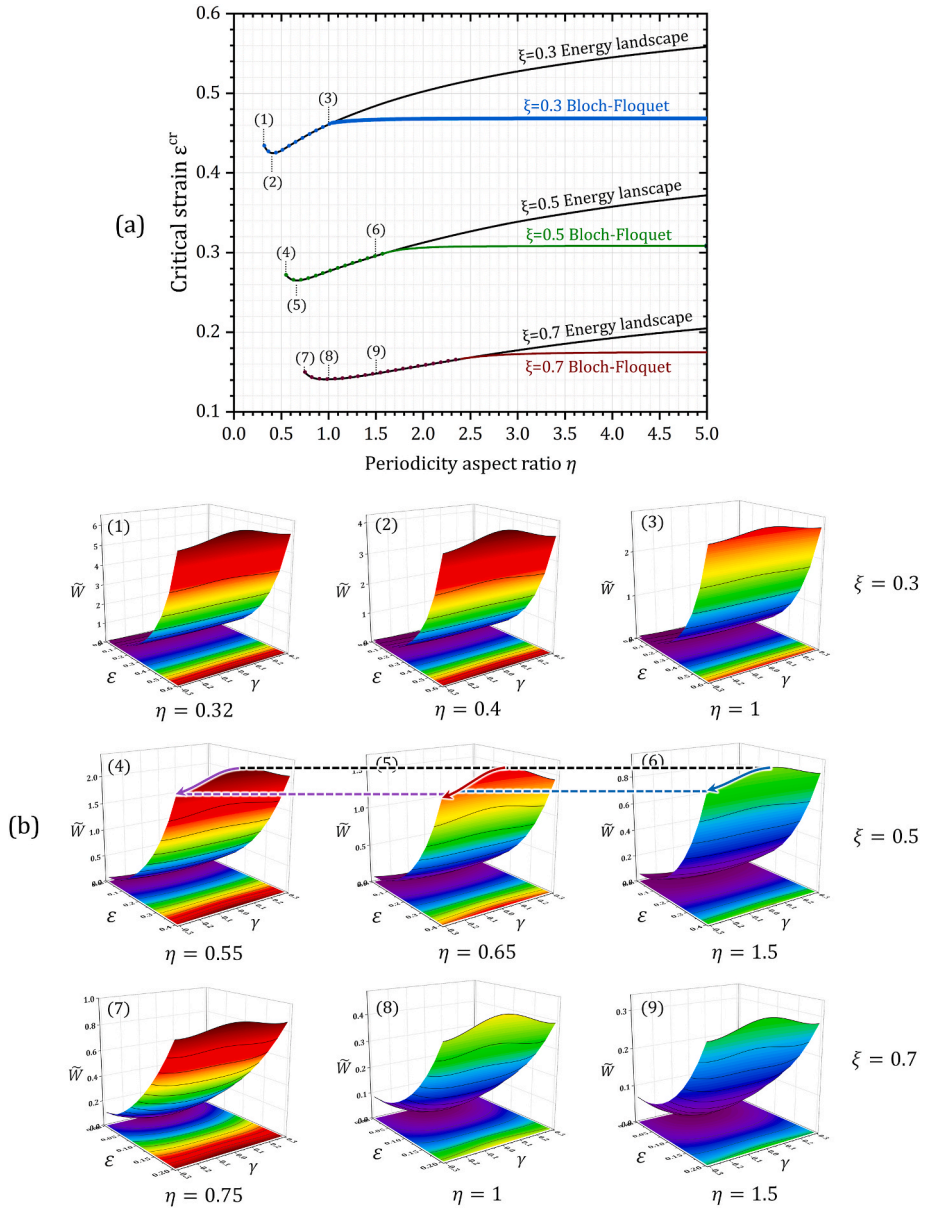


Fig. 9. (a) Comparison of critical strains derived from quasi-convexification and Bloch-Floquet analyses for the composites with $\xi = 0.3$, $\xi = 0.5$, $\xi = 0.7$ and $\xi < \eta \leq 5$; (b) The energy landscapes of the composites with different geometric parameters ($\xi = 0.3$ with $\xi = 0.32$, $\xi = 0.4$, $\xi = 1$; $\xi = 0.5$ with $\xi = 0.55$, $\xi = 0.65$, $\xi = 1.5$; $\xi = 0.7$ with $\xi = 0.75$, $\xi = 1$, $\xi = 1.5$).

dotted curves in Fig. 9a corresponding to $\xi = 0.5$ within $0.5 < \eta < 1.65$). The predictions, however, diverge from each other at the region where microscopic instability occurs first. The threshold values η^{th} corresponds to the transition from longwave to microscopic instability.

Fig. 9b illustrates the transition of the energy landscapes corresponding to the composite configurations (1)–(6) in Fig. 9a. The illustrated energy landscapes (1), (4), and (7) correspond to the lowest values of η, in particular, $\eta = 0.32$, $\eta = 0.55$ and $\eta = 0.75$, respectively; the energy landscapes (2), (5) and (8) correspond to $\eta = 0.4$, $\eta = 0.65$ and $\eta = 1.0$, respectively, at which the curves have their local minima. The energy landscapes (3), (6), and (9) illustrate the composite behavior in the region of increasing ε^{cr}; in particular, $\eta = 1$, $\eta = 1.5$ and $\eta = 1.5$, respectively. In the unstable region, the energy function becomes non-convex, exhibiting a negative energy change rate (with a change in γ), $\partial \widetilde{W}/\partial\gamma < 0$. We note that the composites with a higher rate of energy decrease (at the same level of deformation) are characterized by lower critical strains. This is illustrated in Fig. 9b by the comparison of the composite configurations (4), (5), and (6) having the same spacing ratio $\xi = 0.5$ with all configurations subjected to the same compressive strain level, $\varepsilon = 0.4$. We note that the magnitude of the global energy decrease may also serve as an indicator of the composite stability similar to the local rate of energy change. For example, let us define the global decrease in energy as $[\widetilde{W}(\gamma = 0) - \widetilde{W}(\gamma = 0.3)]/\widetilde{W}(\gamma = 0)$ at the compressive strain level $\varepsilon = 0.4$. For all considered cases, a higher rate of energy decrease corresponds to a higher ratio of global decrease of energy under a small enough increase in γ. In composite configuration (5), we find a 0.135 decrease of energy with γ increased from 0 to 0.3, while those identified from configurations (4) and (6) are 0.108 and 0.0915, respectively. Composite configuration (5) exhibits the highest rate of energy decrease in the non-convex part of the energy landscape. At the same time, composite configuration (5) has the critical strain $\varepsilon^{cr} = 0.265$, which is in the vicinity of the local minimum of the curve corresponding to $\xi = 0.5$ in Fig. 9a. The critical strains of the composite configuration (4) and (6) are $\varepsilon^{cr} = 0.272$ and $\varepsilon^{cr} = 0.296$, respectively.

Similarly, we also compare other composite configurations with the same spacing ratio in Fig. 9b. For example, for the considered configurations (1), (2), (3) (having the same spacing ratio $\xi = 0.3$) the highest global decrease of energy is found for configuration (2), which is characterized by $\eta = 0.4$. The corresponding periodicity ratio of configuration (2) is found to be in the vicinity of the local minimum (at $\eta \approx 0.4$) of the critical strain curve (see the curve for $\xi = 0.3$ in Fig. 9a). Moreover, if we recall the two particulate system behaviors discussed in Sec. 3.2, configurations (3), (6), (9) also correspond to the soft particulate systems with laminate-like behaviors, configurations (1), (4), (7) correspond to the soft particulate system with additional horizontal interactions, and configurations (2), (5), (7) correspond to the vicinity of the transition point between these two particulate system behaviors.

5. Post buckling analysis

In this part, we perform the numerical post-buckling analysis to examine the pattern transformation in soft particulate composites *after* the instability occurs. In the simulations, we consider a representative volume element (RVE) (Bertoldi et al., 2008) with a large number ($N \geq 80$) of unit cells. The RVE is enclosed by four boundaries (*AB*, *CD*, *AC*, and *BD*), defined by nodes *A*, *B*, *C*, and *D*. We apply the in-plane unidirectional compression to the RVE by imposing the periodic boundary conditions on the two boundary pairs $AB - CD$ and $AC - BD$ via the same definitions in the first step of our Bloch-Floquet analysis (see Eq. (16) Sec. 3.1). As a perturbation to trigger instabilities, a geometrical imperfection is introduced in terms of the slight alternation of the stiff inclusion shape. Specifically, the inclusions are modeled as nearly circular ellipses, where geometrical differences are introduced independently on the major and minor diameter and the position of the center of each inclusion. The geometric deviation is set within $10^{-5}b$.

In Fig. 10a, we show a typical post-buckling configuration of the composite. The example is given for the composite with spacing ratio $\xi = 0.45$ and periodicity aspect ratio $\eta = 1.5$. The composite maintains a straight column of inclusions up to $\varepsilon = 0.338$, after which the inclusion column collapses suddenly; the strain level agrees with the Bloch-Floquet analysis prediction of $\varepsilon^{cr} = 0.338$. Fig. 10a shows the RVE at a higher compressive strain $\varepsilon = 0.348$. We observe that, after the buckling occurs, the initial column of inclusions transforms into a wavy chain of inclusions. This observation agrees with the experiments (Li et al., 2019a) and with the predictions of the Bloch-Floquet analysis. Fig. 10b shows the position of the centers of inclusions in the deformed RVE to illustrate the post-buckling pattern. We observe that the center of inclusions seems to evenly distribute on a harmonic wave with a wavelength equal to the critical wavelength $l^{cr} \approx 6.88$ (see, for example, in Fig. 10b, the inclusions distributed on one period of the wave are marked in a block, where block (1)–(3) correspond to three different periods). However, the number of inclusions in one block is not an integer (see, for example, block (1) in Fig. 10b, there are 6 integral inclusions and a seemingly "0.8 inclusion"). Moreover, the distribution of the inclusions in each block is slightly shifted in comparison to other blocks (see, for example, in Fig. 10b, the first inclusion (from the top) in block (1) seems in tangency with the top boundary; however, the first inclusion in block (2) shifts slightly downward and has a certain distance to the top boundary; moreover, the first inclusion in the block (3) shifts further downward). For comparison, we also plot the eigenmode from the Bloch-Floquet analysis in Fig. 10c. We observe that the actual post-buckling pattern (Fig. 10b) and Bloch-Floquet modes (Fig. 10c) share some similarities in the inclusion distribution, and we both observe a "seemingly non-periodic" post-buckling pattern. This observation is in line with the previous discussion (see Sec. 3.3), relating the mismatch to the critical wavelength corresponding to a non-integer number of inclusions.

Next, we examine the post-buckling development of the transition instability modes predicted by the Bloch-Floquet analysis. In Fig. 11, the upper part shows the dependence of the critical wavenumber on the periodicity aspect ratio with a fixed spacing ratio, $\xi = 0.45$, while the lower part shows the corresponding post-buckling patterns at higher strain levels (after the onset of instability).

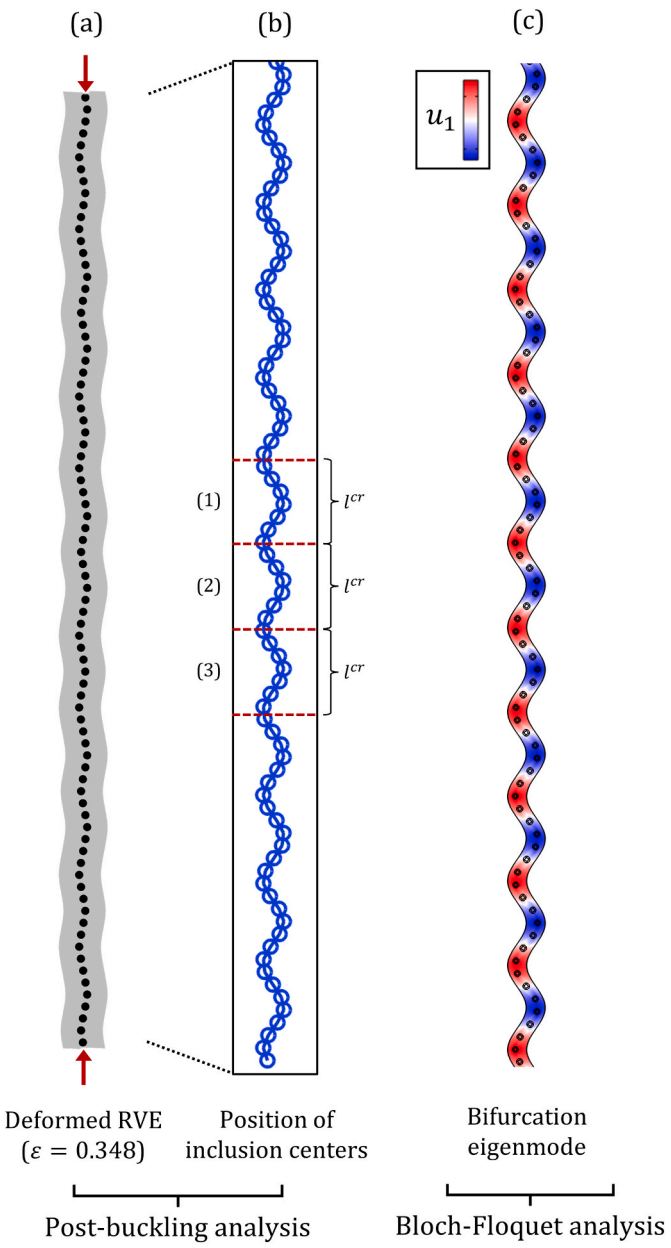


Fig. 10. (a) The deformed RVE under compressive strain $\varepsilon = 0.348$ with initial geometric parameter $\xi = 0.45$ and $\eta = 1.5$; (b) The inclusion center position in the deformed RVE; (c) The corresponding eigenmode (from Bloch-Floquet analysis) of the composite at the critical strain $\varepsilon^{cr} = 0.338$.

We observe an overall transition of the post-buckling patterns from a "zigzag chain" (Fig. 11a) to a "periodicity-doubling pattern" (Fig. 11i); this corresponds to the evolution of the critical wavenumber from the longwave ($k^{cr} \to 0$) to the periodicity-doubling mode ($k^{cr} = 0.5$). First, for the longwave instability mode (see, for example, the pattern in Fig. 11a corresponding to $\eta = 1.4$), we observe a single period of the "zigzag chain" in the deformed RVE. This stems from the fact that the buckling wavelength is much larger than the characteristic size of the microstructure. Therefore, in a finite-sized RVE, we will only observe a single period with a critical wavelength identical to the height of the RVE. Second, when the critical wavenumber starts increasing, the

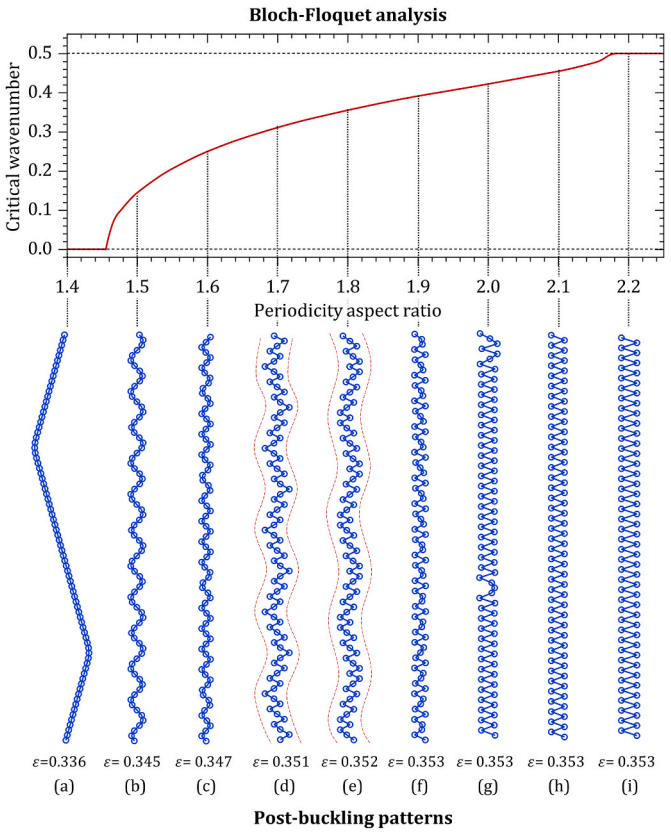


Fig. 11. The transition of post-buckling patterns corresponding to the transition of critical wavenumbers from Bloch-Floquet analysis in the composite with $\xi = 0.45$.

corresponding critical wavelength becomes lower than the height of RVE, and the "wavy chain" emerges in the post-buckling regime (see, for example, the patterns corresponding to $\eta = 1.5$ (b), and $\eta = 1.6$ (c) in Fig. 11). While seemingly agreeing with eigenmode predictions from Bloch-Floquet analysis, these patterns, however, have a slight mismatch of inclusions between wave periods (so that their strict periodicity is pushed towards much large wavelength; this is in line with the discussion in Sec. 3.3). As the critical wavenumber increases beyond $k^{cr} \approx 0.25$, we observe a significant change in the post-buckling shapes (see the shapes corresponding to $\eta = 1.7$ (d) and $\eta = 1.8$ (e) in Fig. 11). These patterns exhibit a superposition of two modes in different wavelengths.

Recall that, in the Bloch-Floquet analysis, for certain wavenumbers larger than 0.25 (see Fig. 6 (1)–(3)), we observed the so-called "beat-like" patterns, reminiscent of a superposition of two modes. However, the difference is that the post-buckling "superposed pattern" has an overall symmetric distribution of inclusions, while the "beat-like" pattern from the Bloch-Floquet analysis has an overall antisymmetric distribution. The reason is that Bloch-Floquet analysis only considers small incremental deformations. Therefore, the large and nonlinear deformations in post-buckling analysis finally lead to a different development of pattern that diverges from the Bloch-Floquet prediction. A further increase in the critical wavenumber (see the pattern corresponding to $\eta = 1.9$ (f) in Fig. 11) leads to the formation of "seemingly chaotic" (much less ordered and lacking periodicity) microstructures in the post-buckling regime. This is due to the fact that the critical wavelength ($l^{cr} \approx 2.91$) corresponds to a very limited number of inclusions (between 2 and 3) that can be accommodated in an enlarged primitive cell. The frustrated composite cannot transform into a periodic structure within the instability-dictated length scale, and hence, it is forced to conform with a combination of inclusion sets in different length scales. The behavior becomes more regulated as the critical wavenumber approach 0.5 (see the pattern corresponding to $\eta = 2.0$ (g) and $\eta = 2.1$ (h) in Fig. 11). These composites take the "periodicity-doubling" post-buckling structure even though their critical wavenumber is not exactly 0.5. Interestingly, as the composite develops the "periodicity-doubling," a localized defect appears (see Fig. 11 corresponding $\eta = 2.0$ (g)). The defects, however, disappear as the critical wavenumber is further increased, and the composite with $\eta = 2.1$ (corresponding to $k^{cr} = 0.455$ in the Bloch-Floquet analysis) exhibits a perfect periodicity doubling without developing the defects in the post-buckling regime (see Fig. 11h). The transition of post-buckling patterns from $\eta = 1.9$ to $\eta = 2.1$ indicates that the composite seeks to develop a periodic structure at a lower length scale, and the periodicity-doubling mode gradually dominates this region. Finally, after the critical wavenumber reaches 0.5, the post-buckling pattern does not change with a further increase in the periodicity aspect ratio η, and the composite develops the periodicity-doubling in the post-buckling regime.

In summary, the post-buckling patterns demonstrate a good agreement with the Bloch-Floquet predictions with a small critical wavenumber (typically, $k^{cr} \leq 0.25$), but the difference appears when critical wavenumber increases beyond $k^{cr} = 0.25$ but not yet reached 0.5. We found, however, at those large wavenumbers, when the composite cannot transform into a periodic structure dedicated by the critical instability wavelength, the pattern is forced to adapt to (i) an inclusion set in the nearby length scale, (ii) a combination of inclusion sets in different length scales, or exhibit (iii) a seemingly chaotic pattern if failing to find an adapt periodic structure. Those adapted patterns, however, were not predicted in Bloch-Floquet analysis since they are completed in a finite deformation after buckling occurs, which is beyond Bloch-Floquet analysis that only predicts small incremental deformations.

6. Conclusion

We have studied the elastic instabilities in soft particulate composites under finite strains. First, we have examined the dependence of the critical strain on geometrical parameters via both the Bloch-Floquet analysis and the quasi-convexification analysis. We find that the composites with higher spacing ratios experience instabilities at lower compressive strains. However, the dependence of the critical strain on the periodicity aspect ratio alters with a change in the spacing ratio. For composites with small spacing ratios, the critical strain ε^{cr} increases monotonically with an increase in η. This behavior, however, changes to a non-monotonic one in the composite with low-to-moderate spacing ratios. The critical strain decreases initially; however, after reaching their local minima, the critical strain increases with a further increase in the periodicity aspect ratio. This non-monotonic dependence indicates two different buckling behaviors in the soft particulate systems. In particular, the composites with large periodicity aspect ratios exhibit the laminate-like buckling behavior; the composites with small enough periodicity aspect ratios experience strong horizontal interactions of neighboring inclusions resulting in the stabilized effect. The transition between these two different soft particulate systems is also illustrated via the corresponding transition of energy landscapes. The predicted critical strain values are in agreement with the Bloch-Floquet analysis in the regime of macroscopic instabilities.

Second, we analyzed the buckling-induced microstructure transformation characterized by the corresponding critical wavenumbers. In particular, the microstructures transform into (i) strictly doubled periodicity, (ii) seemingly non-periodic state, or (iii) longwave pattern. The seemingly non-periodic state occurs with a finite critical wavenumber lower than 0.5 indicating a non-integer number of periods. We note that when the critical wavenumber corresponds to an integer number of periods, the transformed structure achieves a strict periodicity with an integer number of initial primitive unit cells within the updated or enlarged unit cell. However, in the composites with a critical wavenumber corresponding to a non-integer number of periods, the

transformation does not attain a strict periodicity. Instead, it develops in an instability mode at a larger length scale. We illustrated these larger length-scale patterns via the corresponding buckling eigenmodes. Remarkably, some composite morphologies exhibit a beat-like phenomenon – a manifestation of the superposition of the long length-scale instability mode and short wavelets.

Third, we examined the transition of instability modes with geometric parameters. With an increase in the periodicity aspect ratio, the instability mode is found to transit from the longwave mode to the periodicity doubling mode. In particular, (i) for small enough spacing ratios, we found a jump-transition from longwave to periodicity doubling mode with no intermediate instability mode; thus, with no larger scale non-periodic patterns (ii) for moderate spacing ratios, we found a full-transition from longwave to periodicity doubling mode passing through all intermediate instability modes (iii) for large enough spacing ratios, we found a limited-transition from longwave to an intermediate instability mode, but it never reaches the periodicity doubling mode. The reported results may help further develop reconfigurable soft microstructured materials leveraging instability-induced pattern transformations. These material functions include controlling the effective dielectric (Goshkoderia et al., 2020b; O'Neill et al., 2022) or magnetic properties (Pathak et al., 2022) and elastic wave propagation (Arora et al., 2021, 2022) by deformation.

Fourth, we examined the actual post-buckling patterns in soft particulate composites after the instability occurs. The post-buckling patterns seemingly agree with eigenmode predictions from Bloch-Floquet analysis with a critical wavenumber smaller than 0.25, where we observe wavy chain patterns of inclusions. However, for the composites with a critical wavenumber large than 0.25 (but lower than 0.5), the situation changes. At this range of wavenumbers, the composite cannot transform into a periodic structure dictated by the critical wavelength, and the pattern is then forced to adapt to (i) a set with an integer number of inclusions in the nearby length scale, (ii) a combination of inclusion sets of different wavelengths, or exhibit (iii) a seemingly unregulated (chaotic) pattern.

We note that the results are calculated for an idealized composite system and may not account for imperfections stemming from material (Hauseux et al., 2017, 2018; Rappel et al., 2019; Zeraatpisheh et al., 2021) or geometrical (Chen et al., 2019; Ding et al., 2019; Yu et al., 2022) uncertainties. These uncertainties may affect the prediction of the composite buckling behavior. Moreover, interphase between the composite constituents (introduced, for example, in the material manufacturing processes) may influence the instability characteristics (Arora et al., 2019). The influence of such uncertainties can be quantified through multi-field coupled stochastic analyses (Elouneg et al., 2021; Mazier et al., 2022).

Declaration of competing interest

The authors declare that they have no known competing financial interests or personal relationships that could have appeared to influence the work reported in this paper.

Data availability

Data will be made available on request.

Acknowledgements

The authors are grateful for the support of the University of Wisconsin - Madison Office of the Vice Chancellor for Research and Graduate Education with funding from the Wisconsin Alumni Research Foundation.

References

Arora, N., Batan, A., Li, J., Slesarenko, V., Rudykh, S., 2019. On the influence of inhomogeneous interphase layers on instabilities in hyperelastic composites. Materials 12 (5). https://doi.org/10.3390/MA12050763.

Arora, N., Xiang, Y., Rudykh, S., 2021. Multiscale analysis of elastic waves in soft materials: from molecular chain networks to fiber composites. Int. J. Mech. Sci. 200, 106433 https://doi.org/10.1016/j.ijmecsci.2021.106433.

Arora, N., Yao, Q., Rudykh, S., 2022. Deformation activated negative group velocity state in soft laminates. Extreme Mechanics Letters 51, 101592. https://doi.org/10.1016/J.EML.2021.101592.

Bertoldi, K., Boyce, M.C., Deschanel, S., Prange, S.M., Mullin, T., 2008. Mechanics of deformation-triggered pattern transformations and superelastic behavior in periodic elastomeric structures. J. Mech. Phys. Solid. 56 (8), 2642–2668. https://doi.org/10.1016/j.jmps.2008.03.006.

Bruno, D., Greco, F., Lonetti, P., Blasi, P.N., Sgambitterra, G., 2010. An investigation on microscopic and macroscopic stability phenomena of composite solids with periodic microstructure. Int. J. Solid Struct. 47 (20), 2806–2824. https://doi.org/10.1016/J.IJSOLSTR.2010.06.013.

Chen, L.L., Lian, H., Liu, Z., Chen, H.B., Atroshchenko, E., Bordas, S.P.A., 2019. Structural shape optimization of three dimensional acoustic problems with isogeometric boundary element methods. Comput. Methods Appl. Mech. Eng. 355, 926–951. https://doi.org/10.1016/j.cma.2019.06.012.

Conti, S., 2008. Quasiconvex functions incorporating volumetric constraints are rank-one convex. J. Math. Pure Appl. 90 (1), 15–30. https://doi.org/10.1016/J.MATPUR.2008.04.009.

Ding, C., Deokar, R.R., Ding, Y., Li, G., Cui, X., Tamma, K.K., Bordas, S.P.A., 2019. Model order reduction accelerated Monte Carlo stochastic isogeometric method for the analysis of structures with high-dimensional and independent material uncertainties. Comput. Methods Appl. Mech. Eng. 349, 266–284. https://doi.org/10.1016/j.cma.2019.02.004.

El Hamdaoui, M., Merodio, J., Ogden, R.W., 2018. Deformation induced loss of ellipticity in an anisotropic circular cylindrical tube. J. Eng. Math. 109 (1), 31–45. https://doi.org/10.1007/S10665-017-9904-Z/FIGURES/9.

Elouneg, A., Sutula, D., Chambert, J., Lejeune, A., Bordas, S.P.A., Jacquet, E., 2021. An open-source FEniCS-based framework for hyperelastic parameter estimation from noisy full-field data: application to heterogeneous soft tissues. Comput. Struct. 255 https://doi.org/10.1016/j.compstruc.2021.106620.

Ferrari, V., Gatti, P., 1999. Applied structural and mechanical vibrations. In: Applied Structural and Mechanical Vibrations. CRC Press. https://doi.org/10.4324/9780203014554.bmatt.

Galich, P.I., Slesarenko, V., Li, J., Rudykh, S., 2018. Elastic instabilities and shear waves in hyperelastic composites with various periodic fiber arrangements. Int. J. Eng. Sci. 130, 51–61. https://doi.org/10.1016/J.IJENGSCI.2018.05.003.

Gao, N., Li, J., Bao, R.H., Chen, W.Q., 2019. Harnessing uniaxial tension to tune Poisson's ratio and wave propagation in soft porous phononic crystals: an experimental study. Soft Matter 15 (14), 2921–2927. https://doi.org/10.1039/C8SM02468E.

Geymonat, G., Müller, S., Triantafyllidis, N., 1993. Homogenization of nonlinearly elastic materials, microscopic bifurcation and macroscopic loss of rank-one convexity. Arch. Ration. Mech. Anal. 122 (3), 231–290.

Goshkoderia, A., Chen, V., Li, J., Juhl, A., Buskohl, P., Rudykh, S., 2020a. Instability-induced pattern formations in soft magnetoactive composites. Phys. Rev. Lett. 124 (15), 1–7. https://doi.org/10.1103/PhysRevLett.124.158002.

Goshkoderia, A., Arora, N., Slesarenko, V., Li, J., Chen, V., Juhl, A., Buskohl, P., Rudykh, S., 2020b. Tunable permittivity in dielectric elastomer composites under finite strains: periodicity, randomness, and instabilities. Int. J. Mech. Sci. 186 https://doi.org/10.1016/j.ijmecsci.2020.105880.

Greco, F., Luciano, R., 2011. A theoretical and numerical stability analysis for composite micro-structures by using homogenization theory. Compos. B Eng. 42 (3), 382–401. https://doi.org/10.1016/J.COMPOSITESB.2010.12.006.

Greco, F., Leonetti, L., De Maio, U., Rudykh, S., Pranno, A., 2021. Macro- and micro-instabilities in incompressible bioinspired composite materials with nacre-like microstructure. Compos. Struct. 269 https://doi.org/10.1016/j.compstruct.2021.114004.

Hauseux, P., Hale, J.S., Bordas, S.P.A., 2017. Accelerating Monte Carlo estimation with derivatives of high-level finite element models. Comput. Methods Appl. Mech. Eng. 318, 917–936. https://doi.org/10.1016/j.cma.2017.01.041.

Hauseux, P., Hale, J.S., Cotin, S., Bordas, S.P.A., 2018. Quantifying the uncertainty in a hyperelastic soft tissue model with stochastic parameters. Appl. Math. Model. 62, 86–102. https://doi.org/10.1016/j.apm.2018.04.021.

Li, J., Rudykh, S., 2019b. Tunable microstructure transformations and auxetic behavior in 3D-printed multiphase composites: the role of inclusion distribution. Compos. B Eng. 172, 352–362. https://doi.org/10.1016/J.COMPOSITESB.2019.05.012.

Li, Y., Kaynia, N., Rudykh, S., Boyce, M.C., 2013. Wrinkling of interfacial layers in stratified composites. Adv. Eng. Mater. 15 (10), 921–926. https://doi.org/10.1002/ADEM.201200387.

Li, J., Slesarenko, V., Galich, P.I., Rudykh, S., 2018a. Instabilities and pattern formations in 3D-printed deformable fiber composites. Compos. B Eng. 148 (January), 114–122. https://doi.org/10.1016/j.compositesb.2018.04.049.

Li, J., Slesarenko, V., Rudykh, S., 2018b. Auxetic multiphase soft composite material design through instabilities with application for acoustic metamaterials. Soft Matter 14 (30), 6171–6180. https://doi.org/10.1039/C8SM00874D.

Li, J., Pallicity, T.D., Slesarenko, V., Goshkoderia, A., Rudykh, S., 2019a. Domain formations and pattern transitions via instabilities in soft heterogeneous materials. Wiley Online Library 31 (14), 1807309. https://doi.org/10.1002/adma.201807309.

Li, J., Wang, Y., Chen, W., Wang, Y.S., Bao, R., 2019c. Harnessing inclusions to tune post-buckling deformation and bandgaps of soft porous periodic structures. J. Sound Vib. 459, 114848 https://doi.org/10.1016/J.JSV.2019.114848.

Li, J., Slesarenko, V., Rudykh, S., 2019b. Microscopic instabilities and elastic wave propagation in finitely deformed laminates with compressible hyperelastic phases. Eur. J. Mech. Solid. 73 (November 2017), 126–136. https://doi.org/10.1016/j.euromechsol.2018.07.004.

Mazier, A., Bilger, A., Forte, A.E., Peterlik, I., Hale, J.S., Bordas, S.P.A., 2022. Inverse Deformation Analysis: an Experimental and Numerical Assessment Using the FEniCS Project. Engineering with Computers. https://doi.org/10.1007/s00366-021-01597-z.

Melnikov, A., Ogden, R.W., Dorfmann, L., Merodio, J., 2021. Bifurcation analysis of elastic residually-stressed circular cylindrical tubes. Int. J. Solid Struct. 226–227, 111062 https://doi.org/10.1016/J.IJSOLSTR.2021.111062.

Merodio, J., Ogden, R.W., 2002. Material instabilities in fiber-reinforced nonlinearly elastic solids under plane deformation. Arch. Mech. 54 (5–6), 525–552.

Merodio, J., Ogden, R.W., 2003. Instabilities and loss of ellipticity in fiber-reinforced compressible non-linearly elastic solids under plane deformation. Int. J. Solid Struct. 40 (18), 4707–4727. https://doi.org/10.1016/S0020-7683(03)00309-3.

Merodio, J., Ogden, R.W., 2005. Mechanical response of fiber-reinforced incompressible non-linearly elastic solids. Int. J. Non Lin. Mech. 40 (2–3), 213–227. https://doi.org/10.1016/j.ijnonlinmec.2004.05.003.

Merodio, Jose, Pence, T.J., 2001. Kink surfaces in a directionally reinforced neo-Hookean material under plane deformation: I. Mechanical equilibrium. J. Elasticity 62 (2), 119–144. https://doi.org/10.1023/A:1011625509754.

Michel, J.C., Lopez-Pamies, O., Ponte Castaeda, P., Triantafyllidis, N., 2010. Microscopic and macroscopic instabilities in finitely strained fiber-reinforced elastomers. J. Mech. Phys. Solid. 58 (11), 1776–1803. https://doi.org/10.1016/j.jmps.2010.08.006.

Morrey, C.B., 1952. Quasi-convexity and the lower semicontinuity of multiple integrals. Pac. J. Math. https://doi.org/10.2140/pjm.1952.2.25.

Mullin, T., Deschanel, S., Bertoldi, K., Boyce, M.C., 2007. Pattern transformation triggered by deformation. Phys. Rev. Lett. 99 (8) https://doi.org/10.1103/PhysRevLett.99.084301.

Ogden, R., 1997. Nonlinear Elastic Deformations.

O'Neill, M., Sessions, D., Arora, N., Chen, V., Juhl, A., Huff, G., Rudykh, S., Shepherd, R., Buskohl, P., 2022. Dielectric Elastomer Architectures with Strain-Tunable Permittivity. Adv. Mater. Technol., 2200296 https://doi.org/10.1002/ADMT.202200296.

Pathak, P., Arora, N., Rudykh, S., 2022. Magnetoelastic instabilities in soft laminates with ferromagnetic hyperelastic phases. Int. J. Mech. Sci. 213, 106862 https://doi.org/10.1016/J.IJMECSCI.2021.106862.

Rappel, H., Beex, L.A.A., Noels, L., Bordas, S.P.A., 2019. Identifying elastoplastic parameters with Bayes' theorem considering output error, input error and model uncertainty. Probabilist. Eng. Mech. 55, 28–41. https://doi.org/10.1016/j.probengmech.2018.08.004.

Rudykh, S., Boyce, M.C., 2014. Transforming wave propagation in layered media via instability-induced interfacial wrinkling. Phys. Rev. Lett. 112 (3) https://doi.org/10.1103/PHYSREVLETT.112.034301.

Rudykh, S., Debotton, G., 2012. Instabilities of hyperelastic fiber composites: micromechanical versus numerical analyses. J. Elasticity 106 (2), 123–147. https://doi.org/10.1007/S10659-011-9313-X.

Shan, S., Kang, S.H., Wang, P., Qu, C., Shian, S., Chen, E.R., Bertoldi, K., 2014. Harnessing multiple folding mechanisms in soft periodic structures for tunable control of elastic waves. Adv. Funct. Mater. 24 (31), 4935–4942. https://doi.org/10.1002/adfm.201400665.

Slesarenko, V., Rudykh, S., 2016. Harnessing viscoelasticity and instabilities for tuning wavy patterns in soft layered composites. Soft Matter 12 (16), 3677–3682. https://doi.org/10.1039/C5SM02949J.

Slesarenko, V., Rudykh, S., 2017. Microscopic and macroscopic instabilities in hyperelastic fiber composites. J. Mech. Phys. Solid. 99, 471–482. https://doi.org/10.1016/j.jmps.2016.11.002.

Slesarenko, V., Galich, P.I., Li, J., Fang, N.X., Rudykh, S., 2018. Foreshadowing elastic instabilities by negative group velocity in soft composites. Appl. Phys. Lett. 113 (3) https://doi.org/10.1063/1.5042077.

Triantafyllidis, N., Nestorović, M.D., Schraad, M.W., 2006. Failure surfaces for finitely strained two-phase periodic solids under general in-plane loading. J. Appl. Mech. 73 (3), 505–515. https://doi.org/10.1115/1.2126695.

Wang, P., Casadei, F., Shan, S., Weaver, J.C., Bertoldi, K., 2014. Harnessing buckling to design tunable locally resonant acoustic metamaterials. Phys. Rev. Lett. 113 (1), 014301 https://doi.org/10.1103/PhysRevLett.113.014301.

Xiang, Y., Schilling, C., Arora, N., Boydston, A.J., Rudykh, S., 2020a. Mechanical characterization and constitutive modeling of visco-hyperelasticity of photocured polymers. Addit. Manuf. 36 https://doi.org/10.1016/J.ADDMA.2020.101511.

Xiang, Y., Zhong, D., Rudykh, S., Zhou, H., Qu, S., Yang, W., 2020b. A review of physically based and thermodynamically based constitutive models for soft materials. J. Appl. Mech. Trans. ASME 87 (11). https://doi.org/10.1115/1.4047776.

Yu, P., Bordas, S.P.A., Kerfriden, P., 2022. Adaptive Isogeometric analysis for transient dynamics: space–time refinement based on hierarchical a-posteriori error estimations. Comput. Methods Appl. Mech. Eng. 394, 114774 https://doi.org/10.1016/J.CMA.2022.114774.

Zeraatpisheh, M., Bordas, S.P.A., Beex, L.A.A., 2021. Bayesian model uncertainty quantification for hyperelastic soft tissue models. Data Centric Eng. 2 (2) https://doi.org/10.1017/DCE.2021.9.